

HALO MASS FUNCTIONS AT HIGH REDSHIFT

HANNAH O'BRENNAN^{1,*}, JOHN A. REGAN¹, AND CHRIS POWER^{2,3}

¹Centre for Astrophysics and Space Science Maynooth, Department of Physics, Maynooth University, Maynooth, Ireland

²International Centre for Radio Astronomy Research (ICRAR), M468, University of Western Australia, 35 Stirling Hwy, Crawley, WA 6009, Australia

³ARC Centre of Excellence for All Sky Astrophysics in 3 Dimensions (ASTRO 3D)

Version August 28, 2024

ABSTRACT

Recent JWST observations of very early galaxies, at $z \gtrsim 10$, has led to claims that tension exists between the sizes and luminosities of high redshift galaxies and what is predicted by standard Λ CDM models. Here we use the adaptive mesh refinement code `Enzo` and the N-body smoothed particle hydrodynamics code `SWIFT` to compare (semi-)analytic halo mass functions against the results of direct N-body models at high redshift. In particular, our goal is to investigate the variance between standard halo mass functions derived from (semi-)analytic formulations and N-body calculations and to determine what role any discrepancy may play in driving tensions between observations and theory. We find that the difference between direct N-body calculations and halo mass function fits is less than a factor of two within the mass range of galaxies currently being observed by JWST and is therefore not a dominant source of error when comparing theory and observation at high redshift.

1. INTRODUCTION

Since its launch in December 2021 and its subsequent data releases in the months since, JWST has both reshaped and challenged our understanding of galaxy formation in the very early Universe ($z \gtrsim 10$). In particular, JWST has discovered a number of very massive and very luminous galaxies at redshifts in excess of $z = 10$ which after initial photometric detection have now been spectroscopically confirmed (Harikane et al. 2024; Arrabal Haro et al. 2023; Castellano et al. 2024; Hainline et al. 2024; Gentile et al. 2024). These galaxies, both in terms of their intrinsic luminosity and their potential host halo masses, provide a significant challenge to our understanding of structure formation in the early Universe. Boylan-Kolchin (2023) using an analytic model applied to the inferred JWST stellar masses of a number of high redshift source from Labb   et al. (2023) found that the stellar masses implied by the sources required star formation efficiencies, ϵ , significantly in excess of those from the present day universe and perhaps as implausibly high as $\epsilon = 1$. The model employed by Boylan-Kolchin (2023) hinges on a number of simple yet strong assumptions. These assumptions use the inferred stellar host mass to derive a host halo mass based on the ratios between the cosmic baryon density and the cosmic matter density and the star formation efficiency. These simple arguments culminate in a calculation of the probability of finding such (luminous) galaxies at early times in a Λ CDM universe.

Boylan-Kolchin (2023) conclude that the most massive JWST galaxies detected are both at the very limit of galaxy formation theory and that their number densities are difficult to equate with the JWST field of view. They conclude that these issues indicate that there are several unresolved issues in our theories. However, underneath the model employed by Boylan-Kolchin (2023) are a number of astrophysical assumptions which are used

when converting the broadband spectral energy distribution to a host stellar mass. This conversion is open to large uncertainties - particularly since our knowledge of how to do this conversion comes from the local Universe. There is no guarantee that these conversion relations can be directly mapped to the high- z Universe and in fact most analysis shows that it is almost certainly not the case (e.g. Kannan et al. 2023; Lu et al. 2024). For example recent analysis by Steinhardt et al. (2023) show that modifying the host population IMF of the inferred stellar population, results in a decrease in the stellar mass by factors of between 10 and 50. Such decreases in the host stellar mass have a direct knock-on effect to the inferred host halo mass and can significantly decrease the tension with Λ CDM models.

Adding to this important point is that Boylan-Kolchin (2023) (as well as many other studies) utilise the well tested and parameterised halo mass function (HMF) derived by Sheth & Tormen (1999) in order to compute their galaxy number densities and cumulative comoving number density of galaxies. An important consideration therefore is to test, using explicit N-body, calculations how accurate the underlying HMF is at high- z (i.e. at $z \gtrsim 10$), compared to direct N-body calculations, and what error may be associated with this model. This is the goal of this study.

While preparing this work a study by Yung et al. (2024) preformed a similar investigation. Using a high fidelity suite of N-body simulations across a broad range of boxesizes and redshifts Yung et al. (2024) were able to show that HMFs derived from fitting functions and analytical approximations match extremely well to their N-body simulations. Yung et al. (2024) found that even up to $z = 15$ the match between their N-body simulations and the fitting functions is no more than approximately a factor of two across a range of fitting functions. As discussed above, providing robust quantification of the match between fitting functions and direct N-body calculations at high- z is extremely timely given the recent

*E-mail:hannah.obrennan@mu.ie

L [cMpc/h]	$N_{\text{DM}}^{1/3}$	M_{DM} [M_{\odot}/h]
0.5	512	6.69×10^1
1.5	512	1.81×10^3
2.5	512	8.37×10^3
7.5	1024	2.83×10^4
7.5	512	2.26×10^5
12.5	1024	1.31×10^5
12.5	512	1.05×10^6
25.0	1024	1.05×10^6
25.0	512	8.37×10^6
50.0	1024	8.37×10^6
50.0	512	6.70×10^7
100.0	1024	6.70×10^7
100.0	512	5.36×10^8

TABLE 1

MASS RESOLUTIONS OF EACH SIMULATION BOX. ALL SIMULATIONS BUT THE $L = 7.5$ cMpc/h, $N^{1/3} = 1024$ BOX ARE RUN USING BOTH `Enzo` AND `SWIFT`; THIS BOX IS RUN USING `SWIFT` ONLY.

JWST results.

This is particularly relevant when trying to understand the probability of finding such luminous and massive galaxies within a JWST field of view. Thus far several studies have tested the first results from JWST against state-of-the-art hydrodynamical simulations and the results agree within a factor of a few (e.g. [Keller et al. 2023](#); [McCaffrey et al. 2023](#); [Sun et al. 2023](#); [Rennehan 2024](#)). It is therefore timely to quantify potential sources of systematic error when comparing observations and models.

Here we perform a similar analysis to [Yung et al. \(2024\)](#) with the difference being that we compare HMF fitting functions against two fundamentally different numerical codes - `Enzo` ([Bryan et al. 2014](#); [Brummel-Smith et al. 2019](#)) and `SWIFT` ([Schaller et al. 2018, 2024](#)). While [Yung et al. \(2024\)](#) used the publicly available Gadget-2 code [Springel \(2005\)](#) which is a TreePM code, with a similar gravitational solver to `SWIFT` we also use the Particle-Mesh based `Enzo` code which gives an additional layer of comparison. Our analysis confirms the results of [Yung et al. \(2024\)](#) and we also observe a factor of approximately two difference between the HMFs generated by the N-body codes and the fitting functions.

The structure of the paper is as follows: In §2 we outline the methodology including the simulations and fitting functions employed. In §3 we deliver the results of our analysis and in §4 we summarize and discuss our results in light of recent JWST observations.

2. METHODOLOGY

2.1. Numerical simulations

We run a series of dark matter-only simulations using `Enzo` and `SWIFT` of varying resolutions, achieved by varying both the box size and particle number. The box size varies from $L = 0.5$ cMpc/h to 100.0 cMpc/h and the particle number varies from $N_{\text{DM}} = 512^3$ to 1024^3 . Details of the simulation boxes are summarised in Tables 1 and 2.

Our simulations begin at $z = 127.0$ with initial conditions set using MUSIC ([Hahn & Abel \(2011\)](#)) and end at $z = 10.0$. We use a Λ CDM cosmology with $h = 0.6774$, $\Omega_m = 0.2592$, $\sigma_8 = 0.8159$, $n_{\text{eff}} = 0.9667$ and the [Eisenstein & Hu \(1998\)](#) transfer function for no baryon acoustic oscillations. The two codes we use, `Enzo` and `SWIFT`, are both well tested and have been used

L [cMpc/h]	$N_{\text{DM}}^{1/3}$	Δx_{Enzo} [cpc/h]	Δx_{SWIFT} [cpc/h]
0.5	512	7.63×10^0	3.91×10^1
1.5	512	2.29×10^1	1.17×10^2
2.5	512	3.82×10^1	1.95×10^2
7.5	1024	-	2.93×10^2
7.5	512	1.14×10^2	5.86×10^2
12.5	1024	9.54×10^1	4.88×10^2
12.5	512	1.91×10^2	9.77×10^2
25.0	1024	1.91×10^2	9.77×10^2
25.0	512	3.82×10^2	1.95×10^3
50.0	1024	3.82×10^2	1.95×10^3
50.0	512	7.63×10^2	3.91×10^3
100.0	1024	7.63×10^2	3.91×10^3
100.0	512	1.53×10^3	7.81×10^3

TABLE 2

HIGHEST SPACE RESOLUTIONS OF EACH SIMULATION BOX. ALL SIMULATIONS BUT THE $L = 7.5$ cMpc/h, $N^{1/3} = 1024$ BOX ARE RUN USING BOTH `Enzo` AND `SWIFT`; THIS BOX IS RUN USING `SWIFT` ONLY.

extensively within the community. Additionally, both codes use somewhat different strategies for solving the Poisson equation which allows for additional comparison between the various semi-analytic fits against numerical solutions. We now describe both codes but refer the interested reader to the code method papers for more details.

`Enzo` is a grid-based N-body code with the capability for adaptive mesh refinement (AMR), widely used in cosmological hydrodynamics simulations. The AMR allows for improved resolution in areas of interest (e.g. collapsing structures) without greatly increasing computational cost and without needing prior knowledge of the volume to pre-select areas for increased refinement. The gravity solver works by implementing a Fast Fourier Transform (FFT) technique to solve Poisson's equation at the root grid of each timestep of the simulation. The boundary conditions on the subgrids are then interpolated from the parent grid and the Poisson equation is solved at each time step one subgrid at a time. For a unigrid `Enzo` simulation (i.e. no refinement), the minimum inter-particle separation in which gravity acts is twice the length of two cells, given as:

$$\Delta x_{\text{Unigrid}} = 2 \frac{L}{N^{1/3}}. \quad (1)$$

When running `Enzo` simulations, we used a maximum refinement level of 8 meaning that the resolution was increased by a factor 2^8 in regions of high particle density. This means the highest resolution is given as:

$$\Delta x_{\text{Enzo}} = \frac{1}{2^8} \Delta x_{\text{Unigrid}} = \frac{1}{2^7} \frac{L}{N^{1/3}}. \quad (2)$$

For the dark matter only simulations carried out here refinement is triggered once the particle overdensity reaches a factor of 4 greater than the mean density (i.e. `MinimumOverDensityForRefinement` = 4).

In addition to this we set the `MinimumMassForRefinementLevelExponent` = -0.1 which makes the refinement scheme super-Lagrangian and allows for the higher levels of refinement to be more easily triggered. The combination of these parameter choices mean that our simulation setup is somewhat conservative employing an aggressive refinement strategy

(see e.g. O’Shea et al. 2005).

SPH With Inter-dependent Fine-grained Tasking - SWIFT - combines a tree-based N-body solver with a smoothed particle hydrodynamics (SPH) solver. In this study, we use the adaptive mode of the Fast Multipole Method (FMM) (Cheng, Greengard & Rokhlin (1999)). This implements a Taylor expansion twice to resolve the gravitational potential (and later the forces) between particles in different cells. We set the accuracy criterion $\epsilon_{\text{FMM}} = 0.001$. SWIFT takes advantage of the hierarchical tree structure to efficiently solve for the gravitational forces between particles. Particles from nearest neighbour cells are treated as individuals. A group of particles from distant cells are approximated as one particle with the total mass of the group located at the centre of mass. Long-range forces are resolved using a Fast Fourier Transform algorithm (Frigo & Johnson (2005)).

It is a non-trivial matter comparing *Enzo* and SWIFT due to the difference in the gravity solvers. The highest spatial resolution for an *Enzo* simulation, Δx_{Enzo} , applies only to regions of high particle density. The softening length for a SWIFT simulation, Δx_{SWIFT} , applies to the entire simulation volume. We compromise by setting the softening length to an intermediate value, between $\Delta x_{\text{Unigrid}}$ and Δx_{Enzo} :

$$\Delta x_{\text{SWIFT}} = \frac{1}{5^2} \frac{L}{N^{1/3}}. \quad (3)$$

2.2. Numerical Halo Finders

As discussed in §1 the goal of this paper is to determine the differences between (semi-)analytic HMFs and those derived from direct N-body simulations. In order to determine the HMF from the cosmological simulations we must employ a halo finder and decide on the redshifts at which to evaluate the HMFs.

We analyse the simulation snapshots from our full suite of outputs at $z = 20.0$, $z = 15.0$ and $z = 10.0$ using a friends-of-friends (FOF) (Efstathiou et al. (1985)) and HOP halo (Eisenstein & Hut (1998)) finder (results from the HOP finder can be found in the appendix of the paper as the results are very similar between FOF and HOP and the goal of this study is not to compare halo finders). The FOF halo finder accounts for the distances between dark matter particles within a single snapshot. We use a linking length $\Delta x(b) = b \times L/N^{1/3}$, where $L/N^{1/3}$ is the mean inter-particle separation. This refers to the maximum permitted separation between two particles. A group i.e. halo is found from a set of inter-linked particles.

Our halos are approximated as spheres and ideally, we choose b such that each halo encompasses a volume with an overdensity $\Delta_c \approx 18\pi^2$ i.e. 178 times the critical density $\rho_c(z)$ (Bryan & Norman (1998)). The Python package `hmf` (Murray, Power & Robotham 2013) provides an approximation relating Δ_c and b :

$$\Delta_c(z) = \frac{9}{2\pi b^3} \Omega_m(z). \quad (4)$$

As $z \rightarrow \infty$, $\Omega_m(z) \rightarrow 1$ in our cosmology. Therefore, $b = 0.2$ results in a predicted overdensity of $\Delta_c \approx 178$ and this is the value we choose for our FOF algorithm.

The HOP halo finder accounts for the distances between particles as well as the computed density of each particle. Rather than creating a continuous density field in the simulation volume, the density of each particle at its given position is estimated using a spherically symmetric cubic spline kernel (Monaghan & Lattanzio (1985)) on its $N_{\text{dens}} = 64$ nearest neighbours. The density is normalised to the average density of particles within the simulation box e.g. a particle with a computed density of $\delta = 80$ refers to a position 80 times denser than the average i.e. an overdensity (Skory et al. (2010)). A link is made by hopping from a given particle to the densest of its $N_{\text{hop}} = 64$ neighbours. This process continues, forming a chain of increasing particle density until we reach a particle that is its own densest neighbour. All chains sharing the same densest particle are part of the same group. If the maximum particle density within a group is above a set threshold overdensity δ_{peak} , that group is defined as a halo. We use a threshold overdensity of $\delta_{\text{peak}} = 100$. This value was chosen to calibrate the HOP finder with the FOF finder so both halo finders found a similar halo count and mass range for the *Enzo*, $L = 0.5 \text{ cMpc/h}$, $N_{\text{DM}} = 512^3$, $z = 10$ snapshot.

The halo masses found from these halo catalogues are the FOF and HOP masses i.e. the mass of the halo is defined as the sum of the masses of the particles that make up the halos. After we create halo catalogues based on these halo finders, we only include halos made up of at least $N_{\text{DM, min}} = 100$ particles to reduce numerical over-counting (i.e. haloes must be well resolved (by at least 100 particles) before we identify them as haloes).

2.3. Numerical Halo Number Densities

A halo catalogue is created from each snapshot with a specific halo finder using the `yt`¹ and `yt-astro-analysis` packages (Turk et al. (2011), Smith et al. (2022)). An array of halo mass values is generated from each halo catalogue, filtered to exclude halos consisting of $< N_{\text{DM, min}}$ particles. For each array, the halo mass values are binned on a logarithmic scale into 24 histogram bins with $M_{\text{min}} = 10^{3.75} \text{ M}_\odot/\text{h}$ and $M_{\text{max}} = 10^{11.75} \text{ M}_\odot/\text{h}$. Halo catalogues from a given simulation suite, halo finder and redshift, z , are combined, giving rise to 12 datasets (see Table 3 for more detail). For each *Enzo* dataset, we combine halo catalogues based on 12 simulation boxes. For each SWIFT dataset, we combine halo catalogues based on 13 simulation boxes (see Tables 1 and 2 for more detail). In our algorithm below, we index datasets with $i \in \{1, \dots, 12\}$, mass bins with $j \in \{1, \dots, 24\}$, *Enzo* simulation boxes with $k \in \{1, \dots, 12\}$ and SWIFT simulation boxes with $k \in \{1, \dots, 13\}$.

For example, consider the $i = 3$ dataset (*Enzo*, FOF, $z = 10.0$). Say we wish to find the number density $n_{\text{halo, } i=3}^{\text{num}}(M_{\text{mid, } j})$ of the j^{th} bin centred at some mass $\log_{10}(M_{\text{mid, } j}/\text{h}^{-1} \text{ M}_\odot)$. We count the number of halos $N_{\text{halo, } 3,j,k}$ in this bin for each simulation box $\forall k = 1, \dots, 12$ and this specific halo number density is given as:

¹ We use a version of `yt` called `yt-swift` developed by Rennehan (2022) as the most recently available version of `yt` cannot load SWIFT output data.

Simulation	Halo finder	Snapshot	Redshift (z)
Enzo	FOF	20.0	
		15.0	
		10.0	
	HOP	20.0	
		15.0	
		10.0	
SWIFT	FOF	20.0	
		15.0	
		10.0	
	HOP	20.0	
		15.0	
		10.0	

TABLE 3

THE 12 DATASETS DERIVED BY COMBINING HALO CATALOGUES FOR EACH SIMULATION, HALO FINDER AND REDSHIFT COMBINATION.

$$n_{\text{halo}, 3, j, k}^{\text{num}}(M_{\text{mid}, j}) = \frac{N_{\text{halo}, 3, j, k}}{V_k}, \quad (5)$$

where V_k is the comoving volume of the k^{th} simulation box.

We find the halo number density $n_{\text{halo}, 3}^{\text{num}}(M_{\text{mid}, j})$ by averaging over all non-zero number densities across all 12 simulation boxes:

$$n_{\text{halo}, 3}^{\text{num}}(M_{\text{mid}, j}) = \frac{1}{S_{3,j}} \sum_k n_{\text{halo}, 3, j, k}^{\text{num}}(M_{\text{mid}, j}), \quad (6)$$

where $S_{3,j}$ is the number of halo catalogues that found a non-zero halo number density for the j^{th} bin in this dataset.

We can generalise the above equation for the i^{th} dataset and j^{th} bin as:

$$n_{\text{halo}, i}^{\text{num}}(M_{\text{mid}, j}) = \frac{1}{S_{ij}} \sum_k n_{\text{halo}, i, j, k}^{\text{num}}(M_{\text{mid}, j}). \quad (7)$$

2.4. (Semi-)Analytical Halo Mass Functions

We compare our numerical halo number densities with those derived from both analytical forms and popular fits. The number density ($\text{h}^3 \text{cMpc}^{-3}$) of dark matter halos at a given redshift, z , in a mass bin centred at $\log_{10}(M_{\text{mid}}/\text{h}^{-1} \text{M}_\odot)$ with a width of $\Delta \log_{10} M$ is defined as:

$$\begin{aligned} n_{\text{halo}}^{\text{fit}}(z, M_{\text{mid}}) &= \int_{M_a(M_{\text{mid}})}^{M_b(M_{\text{mid}})} \frac{dn}{dM}(z, M) dM, \\ \log_{10} M_a(M_{\text{mid}}) &= \log_{10} \left(\frac{M_{\text{mid}}}{\text{h}^{-1} \text{M}_\odot} \right) - \frac{\Delta \log_{10} M}{2}, \quad (8) \\ \log_{10} M_b(M_{\text{mid}}) &= \log_{10} \left(\frac{M_{\text{mid}}}{\text{h}^{-1} \text{M}_\odot} \right) + \frac{\Delta \log_{10} M}{2}. \end{aligned}$$

The halo mass function ($\text{h}^4 \text{cMpc}^{-3} \text{M}_\odot^{-1}$) is the differential halo number density per unit mass and is defined as:

$$\frac{dn}{dM}(z, M) = \frac{\rho_0}{M^2} f(\sigma(z, M)) \left| \frac{d \ln \sigma(z, M)}{d \ln M} \right|. \quad (9)$$

Here $\rho_0 (\text{h}^2 \text{M}_\odot \text{cMpc}^{-3})$ and $\sigma(z, M)$ refer to the mean density of the universe and mass variance respectively. The mass variance is given as:

$$\sigma^2(z, M) = \frac{1}{2\pi^2} \int_0^\infty k^2 P(z, k) \tilde{W}^2(kR(M)) dk, \quad (10)$$

where $P(z, k)$ is the linear power spectrum and $\tilde{W}(kR)$ is a window function with a filter defined by $R = R(M)$. We use the Top Hat window function given as:

$$\tilde{W}(kR) = \frac{3}{(kR)^3} [\sin(kR) - (kR) \cos(kR)], \quad (11)$$

$$W(r) = \begin{cases} \frac{3}{4\pi R^3} & \text{if } r < R \\ 0 & \text{if } r > R. \end{cases} \quad (12)$$

The linear power spectrum evolves with z as:

$$P(z, k) = d(a(z))^2 P(z = 0, k), \quad (13)$$

where $a(z) = 1/(1+z)$ and $d(a)$ is the normalised linear growth factor (Lukić et al. (2007)) given as:

$$d(a) = \frac{D^+(a)}{D^+(a=1)}, \quad (14)$$

$$D^+(a) = \frac{5\Omega_{m,0}}{2} \frac{H(a)}{H_0} \int_0^a \frac{da'}{[a'H(a')/H_0]^3}. \quad (15)$$

The exact form of $P(z = 0, k)$ depends on the cosmology and the choice of transfer function. Like with our simulations, we initialise the `hmf` objects with the Eisenstein & Hu (1998) transfer function with no baryon acoustic oscillations. The exact form of $f(\sigma(z, M))$ depends on the choice of fitting function for the halo mass function.

2.4.1. Press-Schechter Theory

In Press & Schechter (1974) (PS), a spherical collapse model is assumed for dark matter halos and the probability of reaching a threshold density field value follows a Gaussian distribution. Thus the fitting function for PS is given as:

$$f_{\text{PS}}(\sigma) = \sqrt{\frac{2}{\pi}} \frac{\delta_c}{\sigma} \exp \left(-\frac{\delta_c^2}{2\sigma^2} \right), \quad (16)$$

where $\delta_c \approx 1.686$ is the critical overdensity required for a region to spherically collapse into a dark matter halo. A limitation of the PS fitting function is its tendency to overestimate the number of lower-mass halos and underestimate the number of higher-mass halos compared to N-body simulations (Lacey & Cole (1994), Sheth & Tormen (1999)). Since this seminal paper many other fitting functions have been developed that aim to correct for this discrepancy as well as attempting to add additional sophistication to the modelling. In this work, we explore four other halo mass fitting functions in addition to PS.

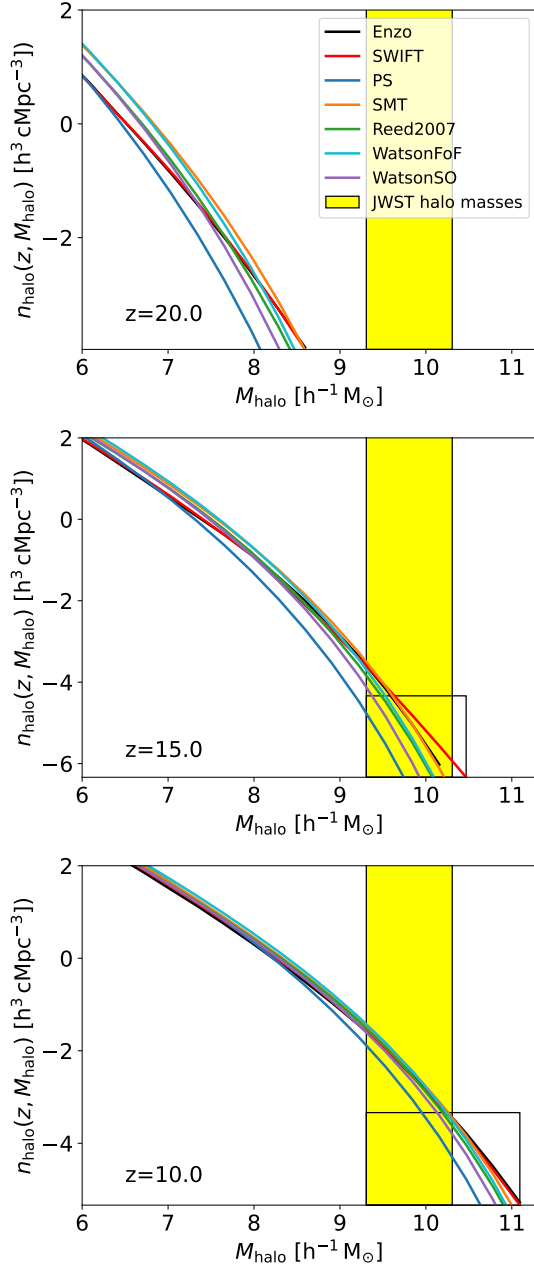


FIG. 1.— Comparing the `Enzo` and `SWIFT` halo number densities with five halo number densities derived from fits (see Table 4) at $z = 20.0$ (upper panel), $z = 15.0$ (centre panel) and $z = 10.0$ (lower panel) using the FOF halo finder. The black rectangles indicate the regions for more detailed analysis as seen in Figure 2. The yellow shaded regions represent the approximate range of halo masses detected by JWST at $z > 10$. Over the halo mass range selected all of the models (both numerical and analytic) agreement at $z = 10.0$ is excellent with some deviation at higher redshift.

2.4.2. Sheth, Mo & Tormen and Beyond

The [Sheth, Mo & Tormen \(2001\)](#) (SMT) halo mass function has a similar form to PS but assumes ellipsoidal collapse and is given as:

$$f_{\text{SMT}}(\sigma) = A \sqrt{\frac{2a}{\pi}} \left[1 + \left(\frac{\sigma^2}{a\delta_c^2} \right)^p \right] \frac{\delta_c}{\sigma} \exp \left(-\frac{a\delta_c^2}{2\sigma^2} \right), \quad (17)$$

where $A = 0.3222$, $a = 0.707$ and $p = 0.3$. We also

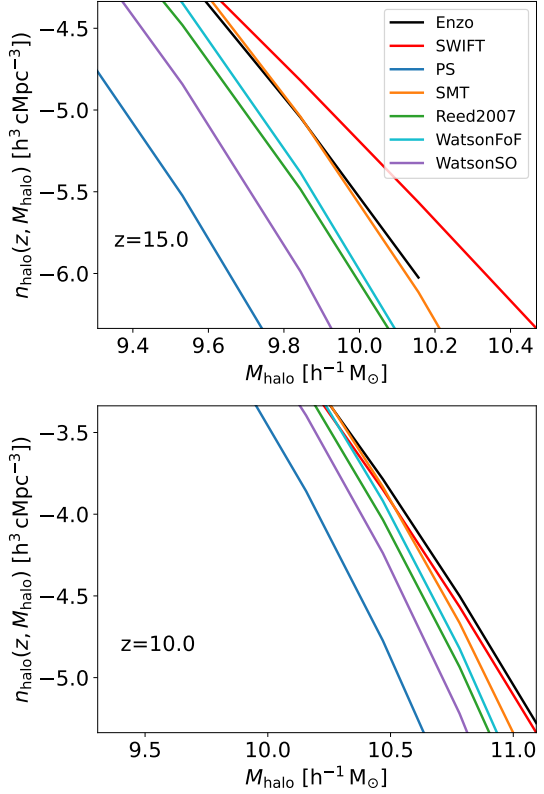


FIG. 2.— A zoom-in onto the black rectangles identified in Figure 1. These mass ranges represent the most massive haloes accessible via numerical simulation at these redshifts. At this higher level of detail we see some discrepancy between the numerical halo mass functions of `Enzo` and `SWIFT` and their (semi-)analytical counterparts, particularly at $z = 15.0$. The residuals for each of the lines is shown in Figure 3 and Figure 4.

Fitting function	z range	Reference
PS	No limit	Press & Schechter (1974)
SMT	No limit	Sheth, Mo & Tormen (2001)
Reed2007	0 - 30	Reed et al. (2007)
WatsonFoF	0 - 30	Watson et al. (2013)
WatsonSO	0 - 30	Watson et al. (2013)

TABLE 4
THE FITTED HALO MASS FUNCTIONS WE USE TO COMPARE TO HMFs DERIVED FROM NUMERICAL SIMULATIONS.

test fitting functions developed by [Reed et al. \(2007\)](#) (Reed07) and [Watson et al. \(2013\)](#) (WatsonFoF refers to a fit using the Friends-of-Friends halo finder, WatsonSO refers to a fit using the Spherical Overdensity halo finder). The PS and SMT fits are widely-used and based on an analytical formalism, with no restriction on redshift or halo mass range. The Reed07, WatsonFoF and WatsonSO fits are based on simulation results, all with a redshift range of $z \in (0, 30)$ and no explicit restriction on halo mass. While many other halo mass fitting functions exist we chose these fits as they were all calibrated across the redshift range of interest to us (i.e. $z > 10$). Other fitting functions are typically calibrated for lower redshifts.

We use the Python package `hmf` to compute halo number densities derived from the HMFs described above.

3. RESULTS

As previously stated the goal of this paper is to compare halo number densities derived from simulation results with those derived from popular fits and to test how well the fits can predict *JWST* halo mass abundances compared to simulations (e.g. [Boylan-Kolchin 2023](#)).

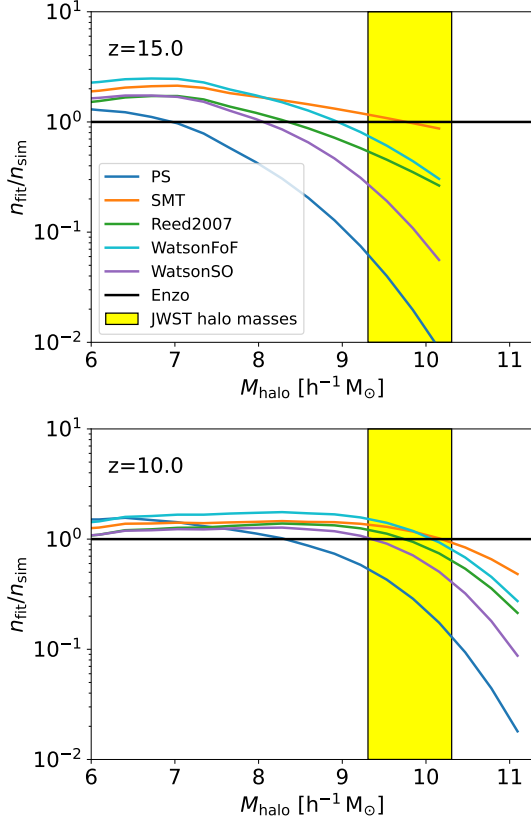


FIG. 3.— The ratios of the fitted halo number densities to the numerical halo number densities, derived from `Enzo` simulations and using the FOF halo finder. Differences between `Enzo` and the (semi-)analytical HMFs are typically less than a factor of two at $z = 10.0$. Increasing only marginally out to $z = 15.0$.

In Figure 1, we compare the HMFs from `Enzo` and `SWIFT` data (dashed lines) with the chosen fits (solid lines) for $z = 20.0$, $z = 15.0$ and $z = 10.0$ using the FOF halo finder. The black rectangles indicate the high mass range depicted in more detail in Figure 2. The range of halo masses selected in the black rectangles is bounded by the approximate lowest halo masses observable by *JWST* at these epochs up to the most massive halo masses accessible by the numerical simulations at that redshift. Given that *JWST* is unlikely to be able to access galaxies at $z \sim 20$ (except perhaps via extreme lensing) we do not add zoom in rectangles for our $z = 20.0$ outputs. Overlaid onto Figure 1 are yellow rectangles which act as a visual aid, depicting an estimate for the range of halo masses that host recently-observed *JWST* galaxies ([Chakraborty et al. 2024](#)). For a given photometric redshift z and stellar mass M_* , we estimate the host halo mass in the usual way:

$$M_{\text{halo}}(z, M_*) = \frac{\Omega_m(z)}{\Omega_b(z)} \frac{M_*}{\epsilon_*}, \quad (18)$$

where we set $\epsilon_* = 0.1$. ϵ_* is the star formation efficiency

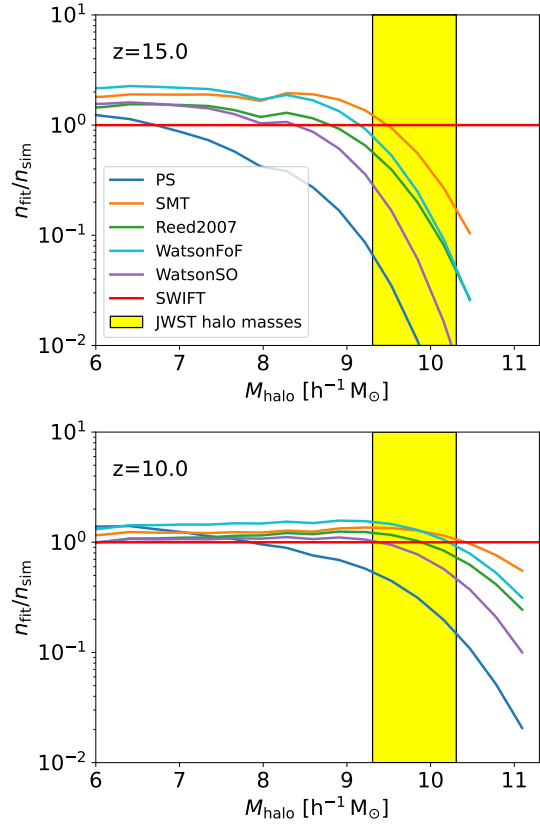


FIG. 4.— The ratios of the fitted halo number densities to the numerical halo number densities, derived from `SWIFT` simulations and using the FOF halo finder. Similar to the `Enzo` result, `SWIFT` shows excellent agreement with the (semi-) analytic HMFs, all fits except PS agreeing within a factor of 2 for all but the highest masses at $z = 10.0$. There is a greater discrepancy present at $z = 15.0$.

parameter.

Over the full mass range, for both simulation suites and halo finders, we find the fits considered agree well across the entire spectrum. There is, over several dexes in mass and over the redshift range between $z = 10.0$ and $z = 20.0$, excellent agreement between all of the HMFs. The largest discrepancies arise at the highest halo masses and the highest redshifts. Aside from the PS fit, the other fits agree closely with numerical simulations - particularly in the *JWST* range at $z = 10.0$, where they agree within a factor of 2. Additionally, the fits improve as redshift decreases - not just between the numerical results and the (semi-)analytic results but even among the (semi-)analytic fits themselves.

As discussed, in Figure 2 we "zoom-into" the black rectangle which spans the range from the lowest *JWST* masses currently observed up to the highest masses accessible via our numerical models. This is only possible for our outputs at $z = 10.0$ and $z = 15.0$ as halo masses large enough to be observed by *JWST* are simply not formed by $z = 20.0$ (in a Λ CDM universe). Hence, we focus our analysis on the $z = 15.0$ and $z = 10.0$ outputs from here on out.

The zoom-in region allows us to see what discrepancies do exist between the numerical HMFs and the (semi-)analytic fits at the masses and redshifts of most interest. At both $z = 15.0$ and $z = 10.0$ the numerical HMFs give a higher number density of haloes than any of the

(semi-)analytic fits. In Figure 2 (top panel), we see a discrepancy between the `Enzo` and `SWIFT` results in the high-mass range at $z = 15.0$. Previous work (e.g. Warren et al. 2006; More et al. 2011) has shown that the FOF mass is sensitive to mass resolution and the presence of substructure, which will be strongly dependent on redshift and which is difficult to correct for in general. It will also depend on local clustering, which can lead to distinct structures being linked by bridges of particles. This is the most likely explanation for the variance between `Enzo` and `SWIFT` at $z = 15.0$. Note that this variance is absent from the HOP profiles (see Figure A.2).

In order to quantify any overall disagreements we make residual plots of all of the data in Figure 3 and Figure 4. In both figures we again show the entire mass range accessible at both redshift $z = 15.0$ and $z = 10.0$. In Figure 3 we show the variation between the `Enzo` simulations and the various (semi-)analytical fits. What we see is that the disagreement between the `Enzo` models and the fits varies between a factor of 2 (at both $z = 10.0$ and $z = 15.0$) and up to a factor of 100 (for the PS semi-analytic). Excluding the PS fits then, we see at most a difference of a factor of two between the `Enzo` (N-body) models and the fits. This is consistent with the results and conclusions of Yung et al. (2024).

In Figure 4 we show the equivalent plot from the `SWIFT` simulation i.e. we take the ratio of the HMF from the `SWIFT` outputs against the (semi-)analytic fits. At $z = 10.0$ the agreement between the numerical (`SWIFT`) results and the analytic fits remains excellent. At $z = 15.0$ we see a strong deviation towards higher masses which was not present for the `Enzo` simulations. It appears here that the `Enzo` runs are better able to resolve haloes at earlier times perhaps due to the inherent refinement strategy. A detailed analysis of the difference between the numerical codes is outside the scope of this paper and comparisons in this direction have been undertaken in the past (e.g. O’Shea et al. 2005; Regan, Haehnelt & Viel 2007; Hayward et al. 2014).

In summary the agreement between the numerical N-body solvers and the (semi-)analytic fits is excellent. In particular, the SMT fitting function gives excellent agreement with `Enzo`, with deviations of at most approximately a factor of two at $z = 15.0$ (for low halo masses which are anyway currently unobservable) and converging to much less than a factor of two within the JWST window. For `SWIFT`, the agreement with SMT is equally excellent at $z = 10.0$ but deviates somewhat for the higher halo masses at $z = 15.0$. Using such (semi-)analytic fits then is unlikely to be a dominant source of error when testing high redshift observations against Λ CMD models.

4. DISCUSSION

The recent explosion of data from the high- z Universe, particularly beyond $z = 10$, by JWST has led to a number of claims that the data is in tension with our galaxy formation and cosmological models (e.g. Boylan-Kolchin 2023; Arrabal Haro et al. 2023; Yung et al. 2024; Finkelstein et al. 2024). The Universe beyond $z = 10$ however is likely to be significantly different to the later and present day Universe. At $z \gtrsim 10$ galaxies are still in their infancy with the most massive galaxies at those epochs having stellar masses less than 10^{10} M_\odot (and would be classified

as dwarfs in the present day Universe). Moreover, there is strong evidence that the astrophysical processes at play at $z = 10$ are sufficiently different to those of the present-day Universe and that they make significant alterations to the galaxy properties. This is particularly evident in galaxies like GN-z11 which is thought to harbour a massive black hole at its centre (Maiolino et al. 2024b), moreover this galaxy contains species abundances which are difficult to explain through standard processes (e.g. Bunker et al. 2023; Cameron et al. 2023; Charbonnel et al. 2023; Nandal et al. 2024). This peculiarity and lack-of-understanding is not unique to GN-z11 with a number of galaxies displaying properties which has evoked confusion within the community (e.g. Maiolino et al. 2024a).

A key part of making progress in understanding the high- z Universe is therefore to identify sources of systematic error in our models at high- z . In this paper we focus on exploring differences in fitting functions to the universal HMF and how they compare against direct N-body simulations at $z > 10$. In particular we compare a wide range of fitting functions in use in the literature (see Table 4) against the adaptive mesh refinement code `Enzo` and against the N-body SPH code `SWIFT`.

We find that for both `Enzo` and `SWIFT` that the match against the SMT analytic functions is excellent and within a factor of two up to $z = 15.0$. The match against the standard Press & Schechter (1974) formalism is less accurate with deviations of up to an order of magnitude (at $z = 10.0$ and $z = 15.0$). Similarly, when comparing against standard fitting formula (see Table 4) we again see good agreement with deviations typically within an order of magnitude up to $z = 15.0$ inside the window in which JWST can approximately observe high- z galaxies.

We caution that the spatial resolution employed, controlled via the softening parameter for `SWIFT` and via the level of maximum refinement with `Enzo`, is set relatively high for our simulations. For example we use a softening length set to approximately the mean inter-particle spacing divided by 25. This is slightly lower to the resolution we evolve the `Enzo` simulations with. This level of gravity resolution, specifically the softening length and spatial resolution here, is likely to be significantly higher than that used for typical galaxy formation simulations designed to run to $z \sim 0$ (e.g. Power et al. 2003, 2016; Zhang et al. 2019). It’s also worth noting that the gravitational collapse of dark matter halos is sensitive to the large scale gravitational field, which in a numerical simulation depends on the size of the simulation volume. Previous work (e.g. Power & Knebe 2006) has highlighted how the mass function is sensitive to simulation volume, with a deficit of halos of a given mass at high masses. This effect is most pronounced in studies of the mass function at high redshifts, where the necessary high mass resolutions and large simulation volumes make these simulations particularly challenging. We therefore caution the reader that matching the results from numerical simulations designed primarily for large scale investigations may struggle to calculate the correct halo properties and abundances at $z \gtrsim 10$ (see e.g. Keller et al. 2023) unless the simulations are truly focused on high- z study (see e.g. McCaffrey et al. 2023).

Nonetheless, overall we find excellent agreement between N-body simulations and both analytic and fitting

functions to HMFs, consistent with the results from [Yung et al. \(2024\)](#), and that these functions are unlikely to lead to large errors in our modelling of high- z host haloes when appropriately modelled.

ACKNOWLEDGEMENTS

JR acknowledges support from the Royal Society and Science Foundation Ireland under grant number

URF\R1\191132 and support from the Irish Research Council Laureate programme under grant number IR-CLA/2022/1165. CP acknowledges the support of the Australian Research Council Centre of Excellence for All Sky Astrophysics in 3 Dimensions (ASTRO 3D), through project number CE170100013.

REFERENCES

Arrabal Haro P. et al., 2023, *Nature*, 622, 707
 Boylan-Kolchin M., 2023, *Nature Astronomy*, 7, 731
 Brummel-Smith C. et al., 2019, *The Journal of Open Source Software*, 4, 1636
 Bryan G. L., Norman M. L., 1998, *The Astrophysical Journal*, 495, 80–99
 Bryan G. L. et al., 2014, *The Astrophysical Journal Supplement Series*, 211, 19, publisher: IOP ADS Bibcode: 2014ApJS..211...19B
 Bunker A. J. et al., 2023, *Astronomy & Astrophysics*, 677, A88
 Cameron A. J., Katz H., Rey M. P., Saxena A., 2023, *MNRAS*, 523, 3516
 Castellano M. et al., 2024, arXiv e-prints, arXiv:2403.10238
 Chakraborty P., Sarkar A., Wolk S., Schneider B., Brickhouse N., Lanzetta K., Foster A., Smith R., 2024, arXiv e-prints, arXiv:2406.05306
 Charbonnel C., Schaerer D., Prantzos N., Ramírez-Galeano L., Fragos T., Kuruvanthodi A., Marques-Chaves R., Gieles M., 2023, *A&A*, 673, L7
 Cheng H., Greengard L., Rokhlin V., 1999, *Journal of Computational Physics*, 155, 468
 Efstathiou G., Davis M., White S. D. M., Frenk C. S., 1985, *The Astrophysical Journal Supplement Series*, 57, 241, publisher: IOP ADS Bibcode: 1985ApJS...57..241E
 Eisenstein D. J., Hu W., 1998, *The Astrophysical Journal*, 496, 605, publisher: IOP ADS Bibcode: 1998ApJ...496..605E
 Eisenstein D. J., Hut P., 1998, *The Astrophysical Journal*, 498, 137, publisher: IOP ADS Bibcode: 1998ApJ...498..137E
 Finkelstein S. L. et al., 2024, *ApJ*, 969, L2
 Frigo M., Johnson S., 2005, *Proceedings of the IEEE*, 93, 216
 Gentile F. et al., 2024, arXiv e-prints, arXiv:2408.10305
 Hahn O., Abel T., 2011, *Monthly Notices of the Royal Astronomical Society*, 415, 2101, arXiv:1103.6031 [astro-ph]
 Hainline K. N. et al., 2024, arXiv e-prints, arXiv:2404.04325
 Harikane Y., Nakajima K., Ouchi M., Umeda H., Isobe Y., Ono Y., Xu Y., Zhang Y., 2024, *ApJ*, 960, 56
 Hayward C. C., Torrey P., Springel V., Hernquist L., Vogelsberger M., 2014, *MNRAS*, 442, 1992
 Kann R. et al., 2023, *MNRAS*, 524, 2594
 Keller B. W., Munshi F., Trebitsch M., Tremmel M., 2023, *ApJ*, 943, L28
 Knebe A. et al., 2011, *MNRAS*, 415, 2293
 Labb   I. et al., 2023, *Nature*, 616, 266
 Lacey C., Cole S., 1994, *Monthly Notices of the Royal Astronomical Society*, 271, 676–692
 Lu S., Frenk C. S., Bose S., Lacey C. G., Cole S., Baugh C. M., Helly J. C., 2024, arXiv e-prints, arXiv:2406.02672
 Luki   Z., Heitmann K., Habib S., Bashinsky S., Ricker P. M., 2007, *ApJ*, 671, 1160
 Maiolino R. et al., 2024a, arXiv e-prints, arXiv:2405.00504
 Maiolino R. et al., 2024b, *Nature*, 627, 59
 McCaffrey J., Hardin S., Wise J. H., Regan J. A., 2023, *The Open Journal of Astrophysics*, 6, 47
 Monaghan J. J., Lattanzio J. C., 1985, *A&A*, 149, 135
 More S., Kravtsov A. V., Dalal N., Gottl  ber S., 2011, *ApJS*, 195, 4
 Murray S. G., Power C., Robotham A. S. G., 2013, *Astronomy and Computing*, 3, 23, aDS Bibcode: 2013A&C.....3...23M
 Nandal D., Regan J. A., Woods T. E., Farrell E., Ekstr  m S., Meynet G., 2024, *A&A*, 683, A156
 O’Shea B. W., Nagamine K., Springel V., Hernquist L., Norman M. L., 2005, *ApJS*, 160, 1
 Power C., Knebe A., 2006, *MNRAS*, 370, 691
 Power C., Navarro J. F., Jenkins A., Frenk C. S., White S. D. M., Springel V., Stadel J., Quinn T., 2003, *MNRAS*, 338, 14
 Power C., Robotham A. S. G., Obreschkow D., Hobbs A., Lewis G. F., 2016, *MNRAS*, 462, 474
 Press W. H., Schechter P., 1974, *The Astrophysical Journal*, 187, 425, publisher: IOP ADS Bibcode: 1974ApJ...187..425P
 Reed D. S., Bower R., Frenk C. S., Jenkins A., Theuns T., 2007, *Monthly Notices of the Royal Astronomical Society*, 374, 2, publisher: OUP ADS Bibcode: 2007MNRAS.374....2R
 Regan J. A., Haehnelt M. G., Viel M., 2007, *MNRAS*, 374, 196
 Rennehan D., 2022, *yt-swift/yt at main · rennehan/yt-swift*
 Rennehan D., 2024, arXiv e-prints, arXiv:2406.06672
 Schaller M., Gonnet P., Draper P. W., Chalk A. B. G., Bower R. G., Willis J., Hausammann L., 2018, *Astrophysics Source Code Library*, ascl:1805.020, aDS Bibcode: 2018ascl.soft05020S
 Schaller M. et al., 2024, *Monthly Notices of the Royal Astronomical Society*, publisher: OUP ADS Bibcode: 2024MNRAS.tmp..925S
 Sheth R. K., Mo H. J., Tormen G., 2001, *Monthly Notices of the Royal Astronomical Society*, 323, 1
 Sheth R. K., Tormen G., 1999, *MNRAS*, 308, 119
 Skory S., Turk M. J., Norman M. L., Coil A. L., 2010, *ApJS*, 191, 43
 Smith B. et al., 2022, *yt-project/yt_astro_analysis: yt_astro_analysis version 1.1.1 is released!*
 Springel V., 2005, *MNRAS*, 364, 1105
 Steinhardt C. L., Kokorev V., Rusakov V., Garcia E., Sneppen A., 2023, *ApJ*, 951, L40
 Sun G., Faucher-Gigu  re C.-A., Hayward C. C., Shen X., Wetzel A., Cochrane R. K., 2023, *ApJ*, 955, L35
 Turk M. J., Smith B. D., Oishi J. S., Skory S., Skillman S. W., Abel T., Norman M. L., 2011, *The Astrophysical Journal Supplement Series*, 192, 9, publisher: IOP ADS Bibcode: 2011ApJS..192....9T
 Warren M. S., Abazajian K., Holz D. E., Teodoro L., 2006, *ApJ*, 646, 881
 Watson W. A., Iliev I. T., D’Aloisio A., Knebe A., Shapiro P. R., Yepes G., 2013, *Monthly Notices of the Royal Astronomical Society*, 433, 1230–1245
 Yung L. Y. A., Somerville R. S., Nguyen T., Behroozi P., Modi C., Gardner J. P., 2024, *MNRAS*, 530, 4868
 Zhang T., Liao S., Li M., Gao L., 2019, *MNRAS*, 487, 1227

APPENDIX

ALTERNATIVE HALO FINDING TECHNIQUES

In addition to the widely used Friends-of-Friends Halo finding algorithm we also investigated how a different halo finder would impact our results. As discussed in §2 we also use the HOP halo ([Eisenstein & Hut \(1998\)](#)) in our analysis. Using the HOP halo finder we find near identical results to the FOF method and again we see approximately a factor of two difference between HOP and the analytic HMFs at both $z = 10.0$ and $z = 15.0$. The difference between

HOP and the fitting functions varies up to an order of magnitude but similar to the FOF method the agreement is nonetheless still very good - particularly at $z = 10.0$ where differences are typically less than a factor of two. In Figure A.1, Figure A.2, Figure A.3 and Figure A.4 we reproduce the figures from the main text but with the halo finding technique switched to HOP instead of FOF. We see negligible differences between FOF and HOP - a finding supported by other research studies (Knebe et al. 2011).

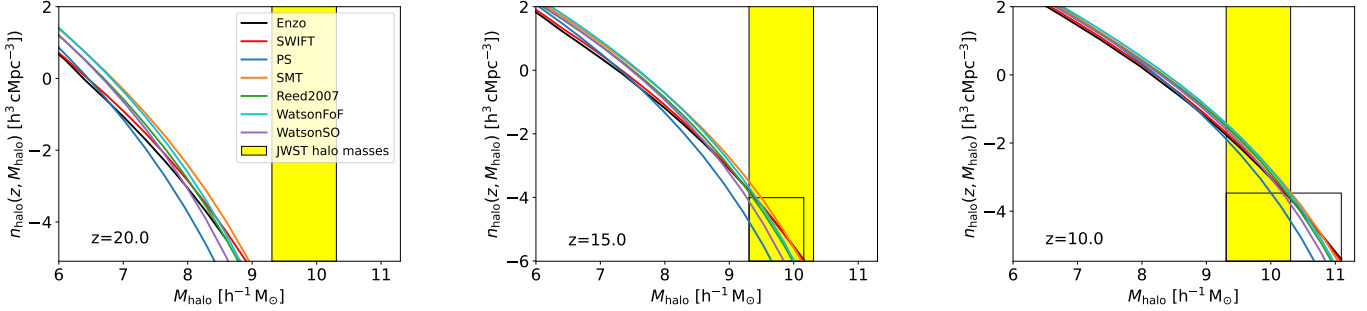


FIG. A.1.— Comparing the Enzo and SWIFT halo number densities contrasted with 5 halo number densities derived from fits at $z = 20.0$ (left panel), $z = 15.0$ (centre panel) and $z = 10.0$ (right panel) using the HOP halo finder.

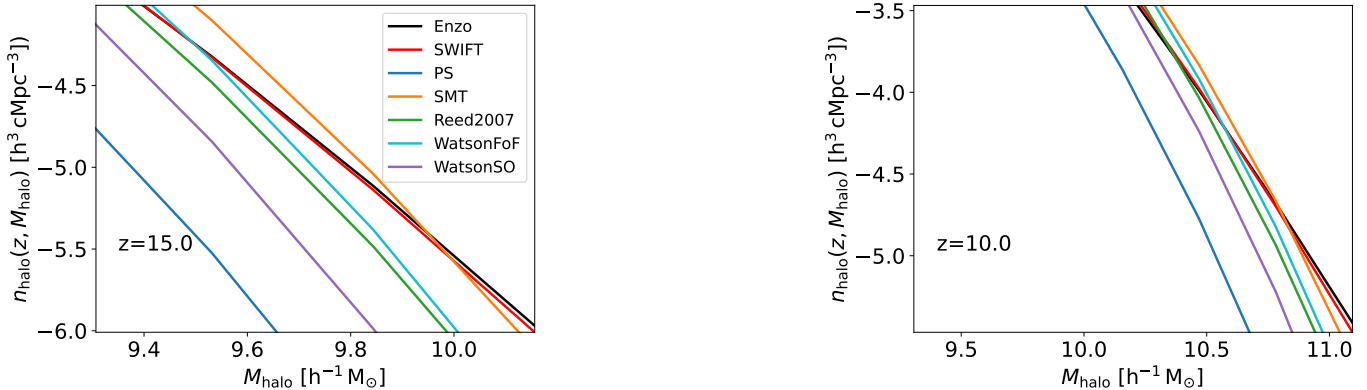


FIG. A.2.— High-mass sections of Figure A.1 (centre and right panels) shown in more detail.

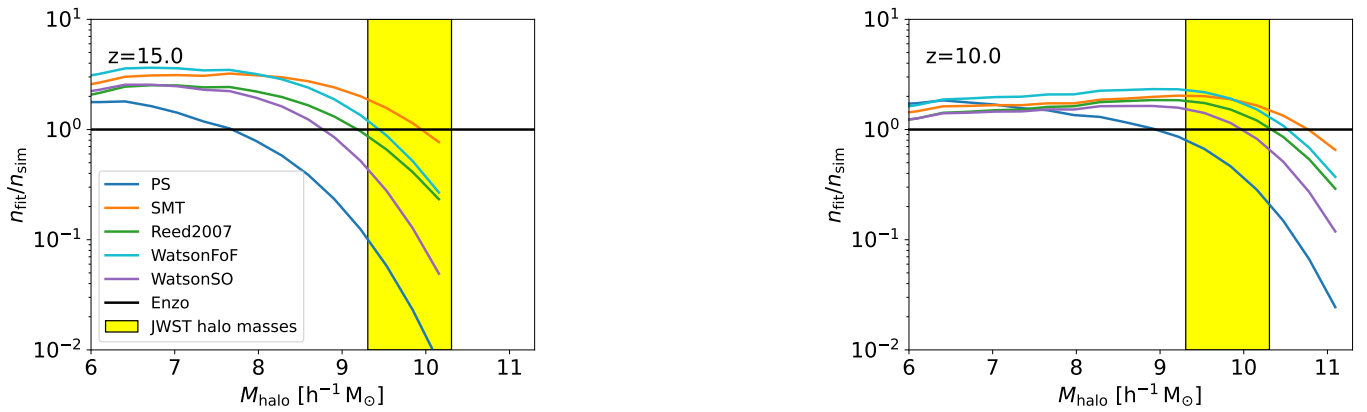


FIG. A.3.— The ratios of the fitted halo number densities to the numerical halo number densities, derived from Enzo simulations and using the HOP halo finder.

This paper was built using the Open Journal of Astrophysics L^AT_EX template. The OJA is a journal which provides fast and easy peer review for new papers in the astro-ph section of the arXiv, making the reviewing process simpler for authors and referees alike. Learn more at <http://astro.theoj.org>.

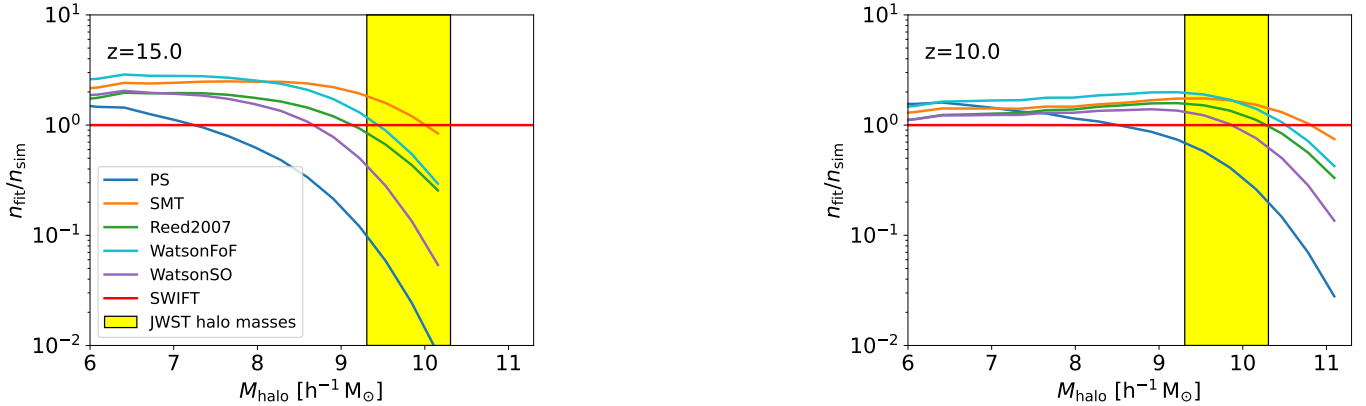


FIG. A.4.— The ratios of the fitted halo number densities to the numerical halo number densities, derived from SWIFT simulations and using the HOP halo finder.